Additive Manufacturing 48 (2021) 102392

Contents lists available at ScienceDirect

Additive Manufacturing

journal homepage: www.elsevier.com/locate/addma

Research paper

Solvent-cast direct-writing as a fabrication strategy for radiopaque stents

Victor Chausse [a,b], Romain Schieber [a], Yago Raymond [a], Brian Ségry [a], Ramon Sabaté [a], Kumaran Kolandaivelu [c,d], Maria-Pau Ginebra [a,b,e], Marta Pegueroles [a,b,*]

[a] Biomaterials, Biomechanics and Tissue Engineering Group, Department of Materials Science and Engineering, Universitat Politècnica de Catalunya (UPC), EEBE, 08019 Barcelona, Spain
[b] Barcelona Research Center in Multiscale Science and Engineering, Universitat Politècnica de Catalunya (UPC), Eduard Maristany, 10-14, 08019 Barcelona, Spain
[c] Massachusetts Institute of Technology, Institute for Medical Engineering and Science, Cambridge, MA 02139, United States
[d] Cardiovascular Division, Brigham and Women's Hospital and Harvard Medical School, Boston, MA 02115, United States
[e] Institute for Bioengineering of Catalonia (IBEC), 08028 Barcelona, Spain

ARTICLE INFO

Keywords:
Solvent-cast direct-writing
Bioresorbable stents
Poly-L-lactic acid
Radiopacity
X-Ray imaging

ABSTRACT

Bioresorbable stents (BRS) potential in treating coronary heart disease is still to be further developed. Current trends include research with new polymeric materials, the need for thinner struts combined with appropriate mechanical properties, radiopacity and optimized local drug delivery. This work presents a novel solvent-cast direct-write (SC-DW) printing system to manufacture BRS onto a rotating cylinder with poly-L-lactic acid (PLLA) and poly(L-lactic-co-ε-caprolactone) (PLCL) inks. Printed stents were characterized in terms of mechanical, thermal and biological properties with human umbilical vein endothelial cells (HUVECs). Expansion assays showed that stents withstood pressures of at least 16 atm and the indirect cytotoxicity test indicated that stents were biocompatible. Polymeric inks were further modified with the addition of 3 radiopaque agents, namely iodine, triiodobenzoic acid (TIBA) and barium sulfate ($BaSO_4$) to render stents radiopaque. Subsequent characterization showed a general increase in strut thickness with respect to control PLLA or PLCL stents, which in turn resulted in higher resistance to compression. Microcomputed tomography was used to assess stents' radiopacity, showing that TIBA and $BaSO_4$-containing stents presented high X-ray attenuation values and maintained their radiopacity after 3 months incubation time.

1. Introduction

Bioresorbable stents (BRS) are designed to solve current permanent stents diseases such as restenosis and late stent thrombosis (LST). BRS should provide a transient support to the vessel allowing it to heal while the structure slowly degrades until completely resorbed [1].

In BRS clinical studies, although Abbott Vascular's Absorb BVS has shown non-inferiority regarding short-term efficacy on post-procedural angiographic results compared to Xience™, a cobalt-chromium drug eluting stent (DES) [2], an increase in stent thrombosis rate was reported in a meta-analysis compiling six trials [3]. Follow-up results after 2 years revealed an increase in major adverse cardiac events [4] and the Absorb was finally withdrawn from the market. The main challenge of BRS development is to find a way of fine tuning the mechanical properties between providing enough vessel support to prevent recoil in the first months after implantation and minimizing the resorption time in order to reduce late undesirable events [5]. The majority of BRS are manufactured with polymers, being poly-L-lactic acid (PLLA) the most used in the field. Despite the potential advantages regarding the use of BRS, they also present a few limitations, such as the need for thicker stent struts in order to achieve sufficient radial strength. Thicker struts might result in more flow disturbance, thus potentially increasing acute thrombotic events [1]. PLLA mechanical properties may be tailored when blending it with other polymers such as poly(ε-caprolactone) (PCL) or the copolymer poly(L-lactic-co-ε-caprolactone) (PLCL). In general, the introduction of increasing amounts of caprolactone results in a decrease in Young's Modulus, a decrease in tensile strength and an increase in elongation at break [6,7]. Nevertheless, the optimal polymer combination to obtain stents with thin struts and enhanced mechanical properties has not yet been elucidated.

* Correspondence to: Universitat Politècnica de Catalunya, Department of Materials Science and Engineering, Av. Eduard Maristany, 10-14, 08019 Barcelona, Spain.
E-mail addresses: victor.chausse@upc.edu (V. Chausse), romain.schieber@upc.edu (R. Schieber), santiago.raymond@upc.edu (Y. Raymond), segry.brian@gmail.com (B. Ségry), ramon.sabate.salvador@gmail.com (R. Sabaté), kkolandaivelu@partners.org (K. Kolandaivelu), maria.pau.ginebra@upc.edu (M.-P. Ginebra), marta.pegueroles@upc.edu (M. Pegueroles).

https://doi.org/10.1016/j.addma.2021.102392
Received 26 May 2021; Received in revised form 10 September 2021; Accepted 4 October 2021
Available online 16 October 2021

In contrast to metallic stents, which are inherently visible under X-ray imaging, BRS lack radiopacity. Consequently, most of the current BRS include radiopaque metallic markers in the device for visibility under X-ray. Although markers can aid in accurate positioning of the scaffold, assessment of scaffold expansion and lesion coverage remains a challenge [1]. Alternatively, radiopaque polymers have been developed, such as an iodinated tyrosine-derived polymer used for the Fantom stents by REVA [8]. Iodine has been used as a radiopaque agent for PCL [9,10], chitosan [11], polymeric nanoparticles [12], electrospun PCL/PLLA fibers [13], injectable poly(ethylene glycol)/polyester thermogel [14,15], α-tocopherol nano-emulsions [16] and degradable poly(vinyl alcohol) hydrogels [17]. Other strategies involve the use of 2,3,5-triiodobenzoic acid (TIBA), an organic-solvent soluble, iodine-based contrast agent, used for PCL modification [18], infused into poly(p-dioxanone) (PPDO) [19] or melt-blended with PPDO and implanted in swine for *in vivo* evaluation [20]. Alternatively, the use of barium sulfate has been reported *in vivo* as a radiopaque agent for PLA urethral stents in rabbits [21], PLA pancreatic stents in rats [22], and PLA biliary stents in pigs [23], showing good biocompatibility. Despite recent advances in radiopaque polymers research, its application to bioresorbable stents is still under development.

Current stent fabrication technologies such as stent braiding or laser machining [24,25] are continuously making progress to develop stents addressed to patients with special needs such as small vessel diameter or diabetes [26,27]. Still, three-dimensional printing (3D Printing) appears as an alternative when personalized medical solutions are required [28]. Unique parts are usually costly and time consuming to produce, but when printers are combined with the 3D imaging techniques already being used by the health industry, this approach becomes viable regarding the potential benefits for the patient [29]. Among 3D Printing techniques, nozzle-based deposition is widely used as a continuous and direct application of the ink through a nozzle to create a 3D pattern layer-by-layer [30]. The ink may be obtained by polymer melting, known as fused-deposition modeling (FDM), or by dissolving the polymer in a solvent and extruding it through pressure-assisted microsyringes, known as solvent-cast direct-writing (SC-DW). SC-DW broadens the range of possibilities regarding stent design and allows for modifications in order to render stents with supplementary features, such as radiopaque BRS.

Recently, there have been advances regarding BRS fabrication by means of different additive manufacturing (AM) approaches such as stereolithography and photopolimerization by exposure to UV light [31], FDM [32–35] or a combination of FDM and post-print crosslinking to develop a biliary stent with $BaSO_4$ coating for X-ray imaging purposes [36]. However, previous approaches involve the use of high temperatures, which may induce polymer degradation and prevent the use of thermally-degradable additives, whereas SC-DW appears as a more flexible technique in terms of ink design. As a proof of concept, Schieber et al. [37] fabricated PLLA bioresorbable stents by SC-DW to assess its feasibility. To the best of our knowledge, a complete characterization of such type of stents has never been reported.

This work presents a versatile AM fabrication strategy for stents by using polymeric inks and direct-writing onto a rotating cylinder. The rheological properties of the PLLA ink in chloroform have been analyzed, and stents with varying geometries have been printed and mechanically tested under compression and expansion tests. Stents were characterized by means of scanning electron microscopy (SEM), differential scanning calorimetry (DSC), thrombogenicity and cytotoxicity assays with human umbilical vein endothelial cells (HUVECs). PLLA and PLCL inks were further modified with the addition of 3 radiopaque agents: (i) iodine, (ii) TIBA and (iii) $BaSO_4$. Radiopaque stents were characterized by means of SEM, DSC and a degradation analysis. Stents' radiopacity was assessed using micro-computed tomography imaging and stents' biocompatibility was evaluated by means of a cytotoxicity assay with HUVECs.

2. Materials and methods

2.1. Chemicals and materials

Medical grade PLLA (Purasorb® PL 65; inherent viscosity $IV = 6.5$ dl/g, M_w=1675000 g/mol) and PLCL (Purasorb® PLC 9538, 95:5 lactic-to-caprolactone molar ratio, $IV = 3.8$ dl/g, M_w=700000 g/mol) were purchased from Corbion (Netherlands). Iodine (>99.99%), TIBA (2,3,5-triiodobenzoic acid, 98%), barium sulfate (99.99%) and chloroform (≥99.5%) were obtained from Sigma-Aldrich (USA).

2.2. Polymer-based ink preparation and characterization

Printable ink was prepared by dissolution of PLLA or PLCL pellets in chloroform at a 10% or 12.5% ratio (w/v), respectively. Polymer dissolution was ensured by means of a Dual Asymmetric Centrifuge (SpeedMixer™, AC 150.1 FVZ, FlackTek, Germany). Obtained ink was introduced in 3cc cartridges (Optimum®, Nordson, USA).

Radiopaque inks consisted of a polymeric solution in chloroform with the addition of a radiopaque agent. Table 1 summarizes all conditions tested, using two polymers as base (PLLA and PLCL), with iodine, TIBA or $BaSO_4$, at different concentrations. $BaSO_4$ was chosen as a positive control for radiopacity assessment. As $BaSO_4$ is not soluble in chloroform, prior to mixing in the centrifuge, sonication in $CHCl_3$ was performed in order to break agglomerates and ensure proper dispersion. Two types of tips (Optimum® SmoothFlow™, Nordson, USA) were used, with internal diameters of 250 μm or 200 μm. Stents printed with the latter are labeled with an asterisk (⋆).

The viscosity of the PLLA and PLCL solutions was evaluated by means of a capillary flow analysis as described in [38,39]. The study consisted in placing the ink in a cartridge with a capillary tip (Nordson, with inner diameter $d_{tip} = 410$ μm and length $l_{tip} = 12.7$ mm), which was extruded at different velocities ($v = 1-60$ mm/s) using a compression setup (Bionix 858 Test System, MTS, USA). The required extrusion force corresponding to each velocity was recorded after reaching steady state.

2.3. 3D Printing of stents

Stents were fabricated by means of SC-DW technique. A commercial FDM 3D printer (BCN 3D+, BCN 3D technologies, Spain) was modified in order to extrude the polymeric solution in chloroform. The printer's y axis was substituted by introducing a rotating mandrel of variable diameter, thus allowing to print cylindrical monolayer structures.

Stents were designed with a structure composed of rhombic cells using Computer-Aided Design (CAD) programme Fusion 360™(Autodesk, USA). Design parameters were stent length (l), stent diameter (d), strut thickness (t), number of peaks (n_p) and number of revolutions (n_r). The parameters n_p and n_r determine mesh density, therefore influencing mechanical properties.

Fig. 1 shows the design scheme of a stent with n_p peaks. The xy plane represents the unfolded cylinder surface, where the x axis corresponds to the longitudinal axis and the y axis unfolds in the rotation direction. Δy stands for the advance in the y axis for a single trajectory in the x axis with length l, and can be calculated from the number of peaks, the number of revolutions and the stent diameter as

$$\Delta y = n_r \pi d + \frac{\pi d}{2n_p} \tag{1}$$

where the first term accounts for the number of revolutions of the rotating cylinder for a single trajectory in the x axis, parametrized by n_r, and the second one for the incremental distance due to the number of peaks, parametrized by n_p. The angle θ can be calculated as

$$\theta = \arctan\left(\frac{\Delta y}{l}\right) \tag{2}$$

Table 1
Overview of inks preparation regarding base polymer, polymer to chloroform ratio, radiopaque agent and its concentration, and printer nozzle diameter. Inks labeled with an asterisk (*) were printed with 200 μm nozzle.

Ink	Polymer	Polymer to chloroform ratio [% w/v]	Radiopaque agent	Concentration [wt.%]	Nozzle diameter [μm]
PLLA	PLLA	10	–	–	250
$PLLA_{1I_2}$	PLLA	10	Iodine	1	250
$PLLA_{5I_2}$	PLLA	10	Iodine	5	250
$PLLA_{10I_2}$	PLLA	10	Iodine	10	250
$PLLA^{*}_{20I_2}$	PLLA	10	Iodine	20	200
$PLLA_{10BaSO_4}$	PLLA	10	$BaSO_4$	10	250
$PLLA_{10TIBA}$	PLLA	10	TIBA	10	250
PLCL	PLCL	12.5	–	–	250
$PLCL_{10BaSO_4}$	PLCL	12.5	$BaSO_4$	10	250
$PLLA^{*}_{20BaSO_4}$	PLCL	12.5	$BaSO_4$	20	200
$PLCL^{*}_{20TIBA}$	PLCL	12.5	TIBA	20	200

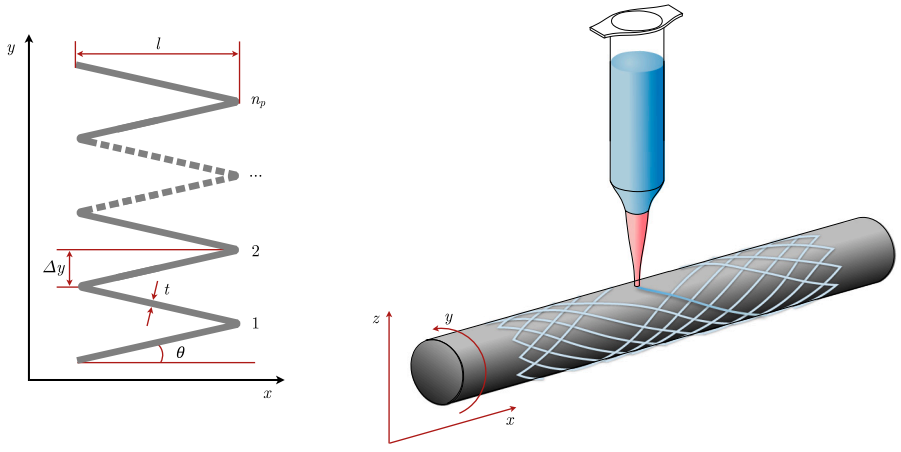

Fig. 1. Design scheme of a stent with n_p peaks and printing setup. The design in the plane xy was printed as a monolayer onto the rotating cylinder's surface.

Stent length was set to 30 mm, n_r was set to 1, stent diameter was determined by the mandrel diameter (3 or 5 mm) and stents were printed with 5, 7, 10, 15 and 20 peaks (labeled as 5p, 7p, 10p, 15p and 20p, respectively). Alternative geometries with varying n_r and n_p values were also obtained. Stents were printed at a velocity of 4 mm/s. Radiopaque stents were fabricated with a fixed design of $n_r = 1$, $n_p = 10$ and 3 mm in diameter. Stents underwent a thermal treatment (TT) after production at 80 °C for 12 h, thus ensuring complete chloroform evaporation [37].

2.4. Stents characterization

2.4.1. Microscopy

Stents were visually examined under optical microscopes Olympus SZX16 and BX51 (Olympus, Japan) and strut thickness was measured using AnalySIS Docu (Olympus, Japan). Results in strut thickness are given as mean ± standard deviation. PLLA stents were coated with platinum–palladium (80:20) and examined under SEM (JEOL JSM-7001F, Jeol, Japan) at 2 kV acceleration voltage. Radiopaque stents were coated with carbon and examined using Phenom XL (Phenom-World, USA) at an operating voltage between 5 and 15 kV.

2.4.2. Differential scanning calorimetry (DSC)

PLLA pellets and stents with and without TT were analyzed by means of a DSC assay (DSC2920, TA instruments, USA). Under a controlled nitrogen atmosphere, samples were heated from room temperature to 250 °C at a rate of 10 °C/min, and maintained at the final temperature for 1 min. From the obtained heat scans, by measuring the area of the melting peak and crystallization peak (if present), one can calculate the crystallinity as

$$\chi_c(\%) = \frac{\Delta H_m + \Delta H_c}{\Delta H_m^0 \times X_{\mathrm{PLLA}}} \times 100 \quad (3)$$

where χ_c is the percentage of the polymer in crystalline form, ΔH_m is the fusion enthalpy of the polymer, ΔH_c is its crystallization enthalpy, X_{PLLA} is the fraction of PLLA in the sample (in mass) and ΔH_m^0 is the theoretical fusion enthalpy of a 100% crystalline PLLA sample, namely 93 J/g [40]. For PLCL stents, crystallinity was calculated with the assumption that lactide units were the only ones to crystallize [7].

2.4.3. Mechanical tests

Radial strength of printed stents was assessed by means of a compression resistance parallel plate test performed with a rheometer (Discovery HR-2, TA instruments, USA). Stents with 3 mm in diameter and n_p = 5, 7, 10, 15 and 20 were tested, before and after undergoing thermal treatment. Stents were compressed up to 50% reduction in diameter between two flat plates, with the upper plate advancing towards the lower one at 1 mm/min, according to ISO 25539-2 [41]. Radial force was measured and normalized by the respective stent length and given in N/mm. Stent elastic recovery was calculated as the ratio between final and initial diameter, in percentage.

Stents were crimped onto a balloon with 3 mm in nominal diameter (MSI HH100/200, Machine Solutions Inc., USA) and deployed into a silicone tube with 3.17 mm in diameter, which corresponds to the average diameter of the aortic artery [42]. Stents' expansion behavior and average breaking pressure were evaluated using mounted stents onto a balloon filled with blue-stained water, in order to facilitate the visualization of broken struts. The balloon was inflated at a rate of 1 atm per 20 s up to 16 atm, which corresponded to the balloon's rated burst pressure (RBP). The pressure at which strut fracture or detachment became visible was noted.

2.4.4. Ex vivo flow setup to evaluate thrombogenicity

To evaluate stent thrombosis with donors' human blood a modified Chandler loop was used, where motor-controlled rotors accelerate blood-filled silicone loops generating pulsatile flow simulating

coronary-like hemodynamics (peak flow, 200 mL/min) at 37 °C [43,44]. To model wall injury, loop segments were made reactive through a 24-hour incubation with 10% bovine type I collagen solution (Beckton Dickinson, USA) and subsequently rinsed with PBS, pH 7.4. The reactive site was composed of three concentric silicone tubes of 3.17 mm, 6.37 mm, and 9.52 mm to generate higher pressure at the place where the stent was deployed (Fig. A.1). The non-reactive part of the loop was loaded with a solution of 2.5% (w/v) bovine serum albumin (Beckton Dickinson, USA) 1-hour prior to the assay and subsequently rinsed with PBS. 3D printed PLLA stents (labeled as PLLA, printed with 250 μm diameter nozzle, and PLLA*, printed with 200 μm diameter nozzle), and a commercial polymeric stent Absorb GT1 stent (Abbott Vascular, USA) were crimped into a 3.0 mm diameter balloon (Abbott Vascular, USA) and balloon expanded up to 16 atm into the reactive segments. Blood was collected from two human healthy donors in 10% acid-citrate-dextrose solution (85 mM trisodium citrate, 69 mM citric acid, 111 mM glucose; pH 4.6). Before use, blood was repleted with a 100 mM $CaCl_2$/75 mM $MgCl_2$ solution with 62.5 μL calcium/magnesium solution per 1 mL blood. Loops were filled, rotor mounted, and run for 4 min to allow in-stent thrombus formation. Free blood was emptied, and reactive segments were isolated and flushed with 120 mL Tyrode solution supplemented with HEPES buffer and magnesium (0.01 mol/L HEPES, 0.75 mM $MgCl_2$). After visual assessment, stented segments were excised and filled with 1% Triton-X solution for 20 min. Equivolume lysates were collected and lactate dehydrogenase (LDH) and hemoglobin (HEM) levels were determined to provide a quantitative measure of total cell/red-cell reflecting thrombogenicity (Cyto-Tox 96 Non-Radioactive Cytotoxicity Assay, Promega Corp; Hemoglobin Colorimetric Detection Kit, Invitrogen, USA) [43,44].

2.4.5. Micro-computed tomography imaging

Stents were scanned in a micro-CT scanner (Skyscan 1272, Bruker, USA). Scans were taken with the following parameters: X-ray tube voltage of 65 kV; anode current of 153 mA; 1 mm Al filter; spatial resolution of pixel size 13 μm; 0.6° rotation step over 180° and scan average $n = 3$. The reconstruction software NRecon (Skyscan, version 1.7.0.4) was used to transform raw micro-CT data into tomographic images in 3D in 8-bit BMP format, with gray level ranging from 0 to 255. Subsequent analysis was performed using CTAn software (Skyscan, version 1.16.9) by segmentation and thresholding to differentiate the sample from the background. Radiopacity was expressed as X-ray attenuation in Houndsfield Units (HU), calculated as the average HU value for each voxel within the sample. HU values were calibrated against a water sample.

2.4.6. Degradation analysis

Among all printed stents, 5 of them were selected to undergo a degradation test: $PLLA_{1I_2}$, $PLLA_{5I_2}$, $PLLA_{10I_2}$, $PLLA_{10TIBA}$ and $PLLA_{10BaSO_4}$. Stents were placed in 20 mL of PBS, and were incubated at 37 °C for 3 months. Afterwards, stents were air dried and stored in a desiccator until further analysis. Radial strength and stents' radiopacity were measured and compared to non-degraded stents.

2.4.7. Cytotoxicity test

The effect of the thermal treatment on PLLA stents was evaluated by means of an indirect cytotoxicity assay following ISO 10993-5 and ISO 10993-12 [45,46] via lactate dehydrogenase (LDH) quantification (Cytotoxicity Detection Kit PLUS, Roche Diagnostic GmbH, Germany). Radiopaque stents' cytotoxicity was assessed via colorimetric Presto Blue (PB) assay (PrestoBlue HS Cell Viability, Invitrogen, Life Technologies). Stents were UV-sterilized, HUVECs were purchased at PromoCell (Germany) and all the experiments were conducted at passages 8 to 10. To calculate cell viability, LDH quantification was performed on a MicroPlate Reader (Synergy HTX multi-mode microplate reader, BioTek Instruments, USA) in absorbance mode, whereas PB was quantified in fluorescence mode.

2.5. Statistical analysis

Each assay condition was tested in triplicate unless stated otherwise and all data are represented as mean values ± standard deviation (SD). Non-parametric Mann–Whitney U-test were used to determine statistically significant differences (p-value < 0.05 between the different groups) and 95% confidence interval (95% CI). Statistical analysis was performed using Minitab software (Minitab Inc., USA).

3. Results

3.1. PLLA ink preparation and characterization

PLLA dissolution in chloroform rendered a transparent, gel-like ink with high viscosity, which was further characterized by means of capillary flow analysis (Fig. 2). The value for n was determined as the slope of the log–log plot of τ_w versus $\dot{\gamma}_{New}$, and found to be 0.2991, as shown in Fig. 2a. The coefficient of determination (R) was very close to 1, therefore ensuring the suitability of the Rabinowitch–Mooney correction in order to account for Non-Newtonian effects [38]. Figs. 2b and 2c present shear stress and viscosity versus shear rate, respectively. A shear-thinning behavior can be observed in the investigated range of printing speeds, as the viscosity decreases for increasing shear rate (Fig. 2d).

3.2. PLLA stents production and characterization

Stents were successfully manufactured onto a rotating cylinder with varying n_r and n_p values, as shown in Fig. 3. Mean strut thickness was found to be 131 ± 9 μm among 3-mm in diameter stents. Struts' area coverage ranged from 16% for 5p stents up to 57% for 20p samples, as shown in Fig. A.2a.

SEM allowed for stents' surface analysis, showing that printed filaments were not completely cylindrical. Filaments were deposited onto the mandrel as solvent evaporation occurred, and therefore they presented a flattened contact face as an unavoidable characteristic of the SC-DW fabrication method. Junctions between two overlapping filaments were welded as shown in Fig. 4a and Fig. 4b, thus ensuring a strong union through extensive contact surface. In contrast to the inner flattened face, stents' outer face presented micropores due to fast solvent evaporation after PLLA filament extrusion (Fig. 4c). A cross-section cut showed no inner porosity (Fig. 4d). Chloroform evaporation resulted in material retraction and surface micropore formation as an inherent feature of the fabrication process. No relevant morphological differences were found when comparing stents before and after thermal treatment, as micropore size and orientation were found to be unaltered.

Stents crystallinity percentage was evaluated by means of DSC (Fig. A.3). PLLA pellets were analyzed as received and found to present a crystallinity of 56.0% ± 5.2%. As expected, a considerable percentage of crystallinity was lost during the conformation process, down to 21.2% ± 1.0% for as-printed stents. Subsequent thermal treatment resulted in a slight crystallinity increase, up to 27.3% ± 1.6%.

Compression tests performed with 3-mm in diameter stents showed a clear difference in mechanical properties among stents (Fig. 5a). For each stent condition, there was a significant increase in resistance to compression force for thermally-treated stents compared to non-treated ones. Moreover, the force needed to compress stents increased with the mesh density, ranging from 0.02 N/mm for thermally-treated stents with $n_p = 5$ up to 0.16 N/mm for thermally-treated stents with $n_p = 20$. Using initial and final diameter, elastic recovery was computed, and found to be around 90% for untreated stents, and around 95% for treated ones, as shown in Fig. 5b. No significant trend was found as the mesh density increased. Stents deployment into silicone tubes showed a good attachment to the inner part of the mock vessel. From $n_p = 5$ to $n_p = 20$, upon balloon deflation and removal, deployed stents remained

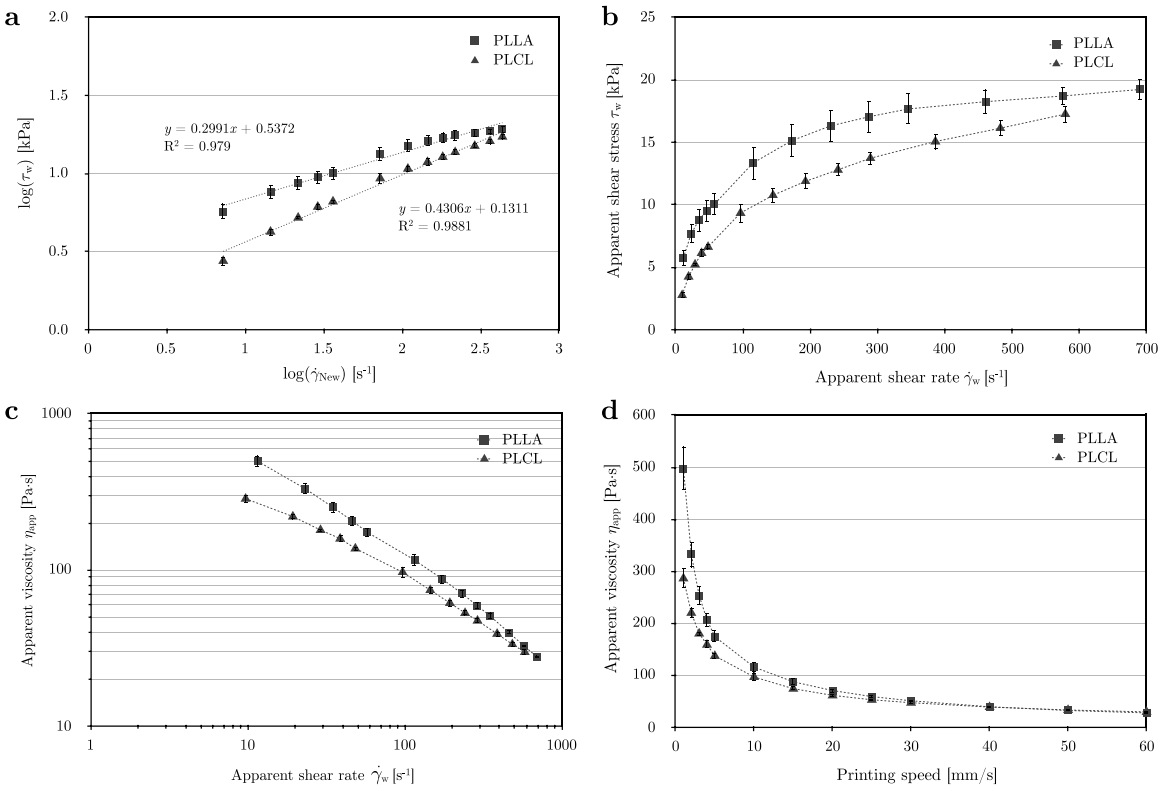

Fig. 2. Rheological curves for PLLA ink. (a) Log–log plot of the process-related shear stress (τ_w) versus the Newtonian shear rate ($\dot{\gamma}_{New}$). (b) Process-related shear stress (τ_w) versus the process-related shear rate ($\dot{\gamma}_w$). (c) Process-related apparent viscosity (η_{app}) plotted as a function of the wall shear rate (τ_w). (d) Process-related apparent viscosity (η_{app}) as a function of printing speed.

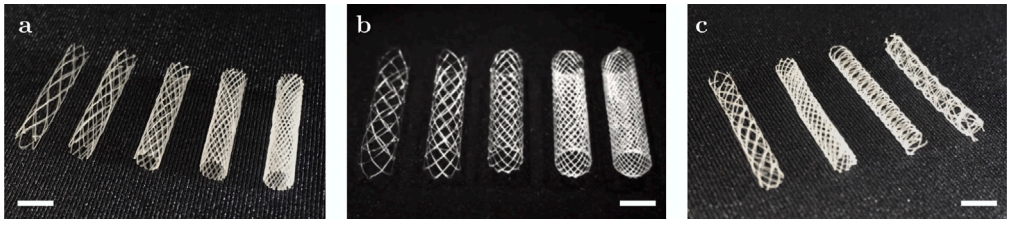

Fig. 3. 3D-printed PLLA stents. (a) Stents with 3 mm in diameter. From left to right, with n_p = 5, 7, 10, 15 and 20. (b) Stents with 5 mm in diameter. From left to right, with n_p = 5, 7, 10, 15 and 20. (c) Other stent geometries achievable with the experimental setup, with different n_r and n_p values. Scale bar corresponds to 5 mm.

attached inside the tube and showed no sign of collapse. Expansion assays showed that stents were able to sustain up to 16 atm (RBP) without any signs of strut breakage (Fig. A.4).

The indirect cytotoxicity test revealed that printed PLLA stents were not cytotoxic for HUVECs. On the one hand, non thermally-treated stents presented a living cell percentage of around 90% for all dilutions, as shown in Fig. A.5. On the other hand, thermally-treated stents exhibited percentages close to or above 100%, therefore indicating that cell growth was similar using complete medium or with pure extract. Considering that the standard indicates that a sample is considered to be toxic for living cell percentages lower than 70% [45], these results manifest the non-toxicity behavior of PLLA SC-DW stents.

The thrombogenicity of printed stents was evaluated using an *ex vivo* flow setup. Tested PLLA stents presented a mean strut thickness of 131 ± 9 μm, whereas PLLA* showed 83 ± 12 μm. In Fig. 6a, the analysis of LDH/HEM for each donor's blood was done to find the relationship between the total amount of adhered cells and the amount of red blood cells involved in clotting processes. Visual differences were observed between the different stents, observing higher red blood cells attachment for PLLA and the commercial stent compared to PLLA* (Fig. 6b). The LDH/HEM ratio quantifies the total number of cells (LDH) vs. the total hemoglobin (HEM) which is directly related to the number of red blood cells involved in the coagulation process. A lower value of LDH/HEM indicates that the proportion of red blood cells to the total number of cell is high and thus, a higher thrombogenicity. Stents with thinner struts were less prone to thrombogenicity, whereas thicker strut stents and the commercial stent showed higher thrombogenicity. Differences among conditions were statistically significant. The LDH/HEM ratio showed similar tendencies independently of the tested patient blood.

3.3. Radiopaque stents production and characterization

Mixing of PLLA pellets, chloroform and radiopaque agent resulted in homogeneous inks with the proper rheological properties. Iodine-containing inks presented a pink color, which increased in intensity with increasing iodine concentration. On the other hand, TIBA-containing inks were pearl white, whereas $BaSO_4$-containing inks were chalk-white, with no visual agglomerates after sonication. $BaSO_4$ size distribution was found to be from 0.75 to 2 μm, with a mean particle size of 1.5 μm. For PLCL-based inks, a higher polymer to solvent ratio was needed in order to match the viscosity shown by the PLLA

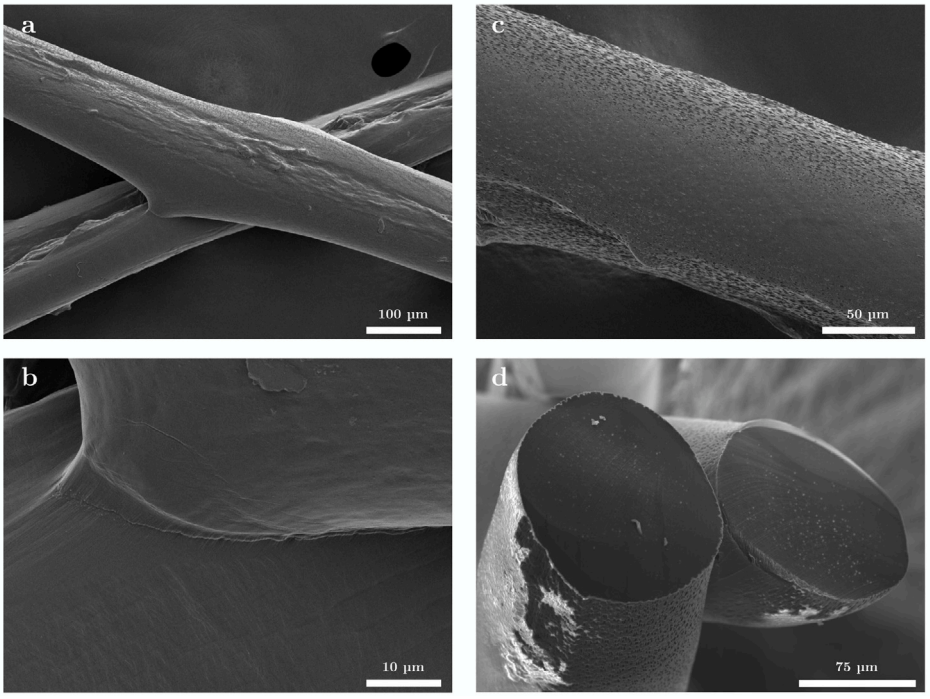

Fig. 4. (a) PLLA stent SEM image of the junction between filaments and (b) detail of weld line. (c) Stent SEM images of the micropores distribution and (d) stent cross-section.

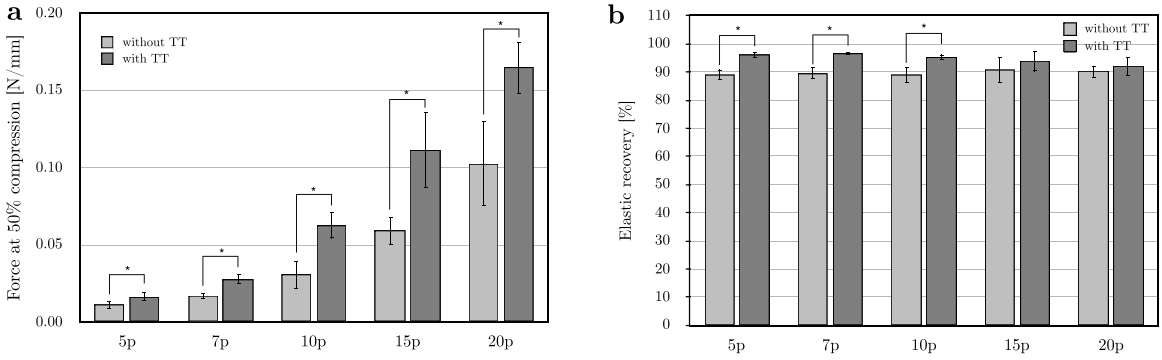

Fig. 5. (a) Compression force at 50% deformation for PLLA stents with increasing mesh density, before and after TT. (b) Elastic recovery shown by stents. Statistically significant differences among conditions are shown with an asterisk ($p < 0.05$).

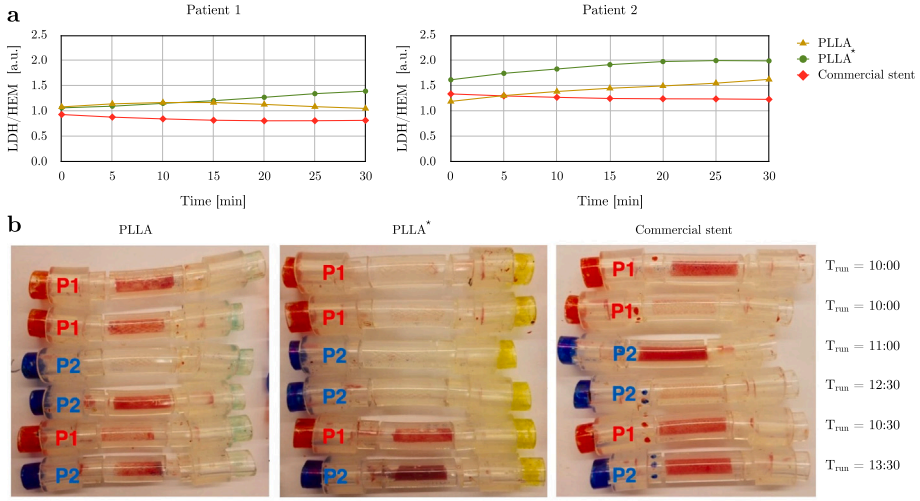

Fig. 6. Thrombogenicity results of 3D printed PLLA stents with different strut thickness and a commercial polymeric stent. (a) Average quantification of the total cells/red cells ratio. (b) Images of the clotting process after a certain period of time (min) for both blood donors (P1 and P2).

Table 2
Stents' strut thickness and crystallinity.

Stent	Strut thickness [μm]	Crystallinity [%]
PLLA	132.2 ± 7.1	27.3 ± 1.6
$PLLA_{1I_2}$	205.3 ± 15.2	24.0 ± 1.4
$PLLA_{5I_2}$	212.6 ± 10.3	25.2 ± 4.4
$PLLA_{10I_2}$	245.3 ± 14.1	35.3 ± 4.3
$PLLA^{\star}_{20I_2}$	124.6 ± 5.0	45.3 ± 9.4
$PLLA_{10BaSO_4}$	208.0 ± 4.1	26.7 ± 1.3
$PLLA_{10TIBA}$	215.2 ± 5.6	31.0 ± 3.3
PLCL	134.0 ± 5.3	21.2 ± 0.8
$PLCL_{10BaSO_4}$	200.8 ± 20.0	22.1 ± 0.6
$PLCL^{\star}_{20BaSO_4}$	178.1 ± 3.1	21.5 ± 0.7
$PLCL^{\star}_{20TIBA}$	161.3 ± 6.6	26.7 ± 1.4

ink. Fig. 2 shows the rheological characterization of PLCL ink. When compared to PLLA ink, a very similar shear-thinning behavior can be observed, although displaying reduced viscosity.

Radiopaque bioresorbable stents were satisfactorily fabricated through SC-DW. Fig. 7 shows three pictures of the 3D printing process for (a) a iodine-containing PLLA stent, (b) a $BaSO_4$-containing PLCL stent and (c) a TIBA-containing PLCL stent.

An overview of all printed conditions can be seen in Fig. A.6. Iodine-containing stents showed a brownish color as the chloroform evaporated. Subsequent thermal treatment resulted in a significant color change. Stents with TIBA and $BaSO_4$ showed no change in color after undergoing TT. Strut thickness for radiopaque stents resulted in an increase with respect to PLLA stents. The addition of iodine, TIBA or $BaSO_4$ led to thicker struts, around 200 μm. The effect was especially manifest for the case of $PLLA_{10I_2}$, with up to 250 μm. The use of a 200 μm diameter nozzle instead of the one with 250 μm allowed for a significant reduction in strut thickness, with 124.6 μ for $PLLA^{\star}_{20I_2}$, 178.1 μm for $PLCL^{\star}_{20BaSO_4}$ and 161.3 μm for $PLCL^{\star}_{20TIBA}$, as shown in Table 2.

Stents were further characterized with SEM. Iodine-containing stents presented a slightly wave-like surface, as one can see in Fig. 8. Stents with $BaSO_4$ showed a homogeneous dispersion of microparticles throughout the filaments and TIBA-containing stents displayed formation of TIBA crystals following the printing direction subsequent to chloroform evaporation. Among all printed radiopaque stents, only $PLLA^{\star}_{20I_2}$ became brittle and showed numerous fractured struts after undergoing TT.

DSC analysis showed that the highest crystallinity was found for $PLLA^{\star}_{20I_2}$ samples, up to 45.3% (Table 2 and Fig. A.3). $PLLA_{10BaSO_4}$ stents presented the same crystallinity as bare PLLA stents, around 27%, whereas $PLLA_{10TIBA}$ showed a higher crystallinity, around 31%. For PLCL-based stents, the addition of 10 wt% or 20 wt% $BaSO_4$ resulted in no change in crystallinity. Finally, as for the PLLA case, $PLCL^{\star}_{20TIBA}$ exhibited a remarkable higher crystallinity with respect to $BaSO_4$ addition.

Mechanical properties of radiopaque stents were evaluated by means of compression and expansion tests. Fig. 9a presents the force-strain curves for all printed stents. PLLA, $PLLA_{1I_2}$, $PLLA_{5I_2}$ and $PLLA_{10TIBA}$ showed a resistance to 50% compression in diameter between 1.5 and 2 N; $PLLA_{10BaSO_4}$, PLCL and $PLCL_{10BaSO_4}$ between 2 and 2.5 N; $PLLA_{10I_2}$ above 3 N and $PLLA^{\star}_{20I_2}$, $PLCL^{\star}_{20BaSO_4}$ and $PLCL^{\star}_{20TIBA}$, below 1 N. The latter 3 conditions were printed with a lower diameter nozzle (200 μm instead of 250 μm). Besides, $PLLA_{10TIBA}$ and $PLLA_{10BaSO_4}$ showed a discontinuous profile, and the latter presented the highest resistance to compression at low deformation. Fig. 9b displays the normalized force at 50% diameter compression (left axis) as well as the computed elastic recovery (right axis). Clearly, stents printed with the smaller diameter nozzle resulted in poorer resistance to compression, whereas it increased with the addition of a radiopaque agent. Elastic recovery was very similar for all cases and found to be around or above 95%. Regarding expansion assays, deployment of radiopaque stents into silicone tubes displayed close attachment to the inner part of the tube. Both PLLA- and PLCL-based radiopaque stents remained attached upon balloon removal, except from $PLLA^{\star}_{20I_2}$, which cracked as pressure increased. Unrestricted expansion assays revealed issues for some conditions. $PLLA_{1I_2}$, $PLLA_{10BaSO_4}$ and $PLLA_{10TIBA}$ stents displayed strut detachment at certain junctions upon balloon inflation. All other conditions showed that stents were able to sustain at least 16 atm (RBP) without strut breakage (Fig. A.7).

Stents were micro-CT scanned in order to evaluate their radiopacity. Fig. 10a presents the resulting reconstruction for all stents. Qualitatively, iodine-containing stents do not seem to appear more highlighted than PLLA or PLCL control stents. On the other hand, there are clear differences among the others, being $BaSO_4$- and TIBA-containing stents the ones with a better visibility. These differences are quantified in Fig. 10b, where X-ray attenuation for each stent is shown in HU values. TIBA appears as the most radiopaque agent, with about 2000 HU for $PLLA_{10TIBA}$ and around 3000 HU for $PLCL^{\star}_{20TIBA}$ when doubling its content. $BaSO_4$ also renders significant radiopacity, around 1600 HU for $PLLA_{10BaSO_4}$ and $PLCL_{10BaSO_4}$, and up to 2500 HU for $PLCL^{\star}_{20BaSO_4}$. Finally, iodine-containing stents show no change in X-ray attenuation with respect to PLLA or PLCL stents, with −250 HU.

Incubated stents in PBS for 3 months at 37 °C were further characterized by means of a compression test and a micro-CT scan. Fig. 11a shows the normalized force at 50% compression. In general, no change in mechanical properties was found after 3 months incubation, except for $PLLA_{10TIBA}$, showing a decrease from 0.096 N/mm to 0.65 N/mm. Regarding elastic recovery, values ranged from 92% for $PLLA_{10TIBA}$ to 96% for $PLLA_{5I_2}$ and $PLLA_{10BaSO_4}$. No statistically significant differences were found with respect to the elastic recovery shown by non-incubated stents. Analysis of microCT scans demonstrated no significant change in X-ray attenuation compared to non-incubated stents, as shown in Fig. 11b. Iodine-containing stents kept around−250 HU, whereas $PLLA_{10BaSO_4}$ and $PLLA_{10TIBA}$ showed similar X-ray attenuation values with respect to non-incubated stents.

Cytotoxicity of 3D-printed radiopaque stents was evaluated via an indirect cytotoxicity assay (Fig. 12). On the one hand, cell viability resulted above 70% for iodine-containing stents, as well as for stents printed with $BaSO_4$, which showed cell viability to be around 80%, for all dilutions. On the other hand, cell viability decreased to around 40% for TIBA-containing stents with pure extract. The effect of the dilutions ($^1/_2$ and $^1/_{10}$) resulted in cell viability close to 100% for $PLLA_{10TIBA}$ and around 70% for $PLCL^{\star}_{20TIBA}$.

4. Discussion

The use of biodegradable polymers as a suitable material for cardiovascular stents has been a recurring idea in the treatment of coronary heart disease. Major advances in this technology have been achieved in the last decade, but still more research is needed to overcome some of the limitations shown by BRS. Here we present a versatile approach for BRS fabrication which circumvents the need of high temperatures, associated to FDM processes as previously shown in the literature [32–35]. SC-DW represents a step forward as it allows for a broad versatility with regards to ink composition and patient-specific customization, both in terms of stent design and functionalization.

PLLA dissolution in chloroform resulted in a viscous, printable polymeric solution. At a printing speed of 4 mm/s, the apparent viscosity has been calculated to be 207 Pa·s. In comparison to other printable ink studies, the extrusion applied pressure range is slightly lower, but the overall rheology of our chloroform-based ink is similar to the one reported in [47], which was based on dichloromethane.

Strut coverage area was measured for 3-mm in diameter stents, showing a range from 16% for 5p stents up to 57% for 20p samples. In comparison to commercial stents, the Absorb presents a surface area coverage of 27% at rated burst pressure, which decreases to 22% for the Magnitude stent [48]. Regarding strut thickness, it was measured to be around 130 μm, which is lower than the strut thickness presented

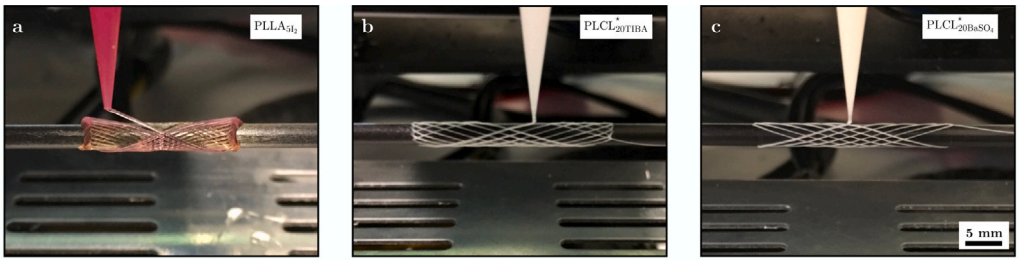

Fig. 7. 3D printing of a radiopaque stent with (a) iodine, (b) $BaSO_4$ and (c) TIBA. (a) was printed with a 250 μm diameter nozzle, whereas for (b) and (c) a 200 μm diameter nozzle was used.

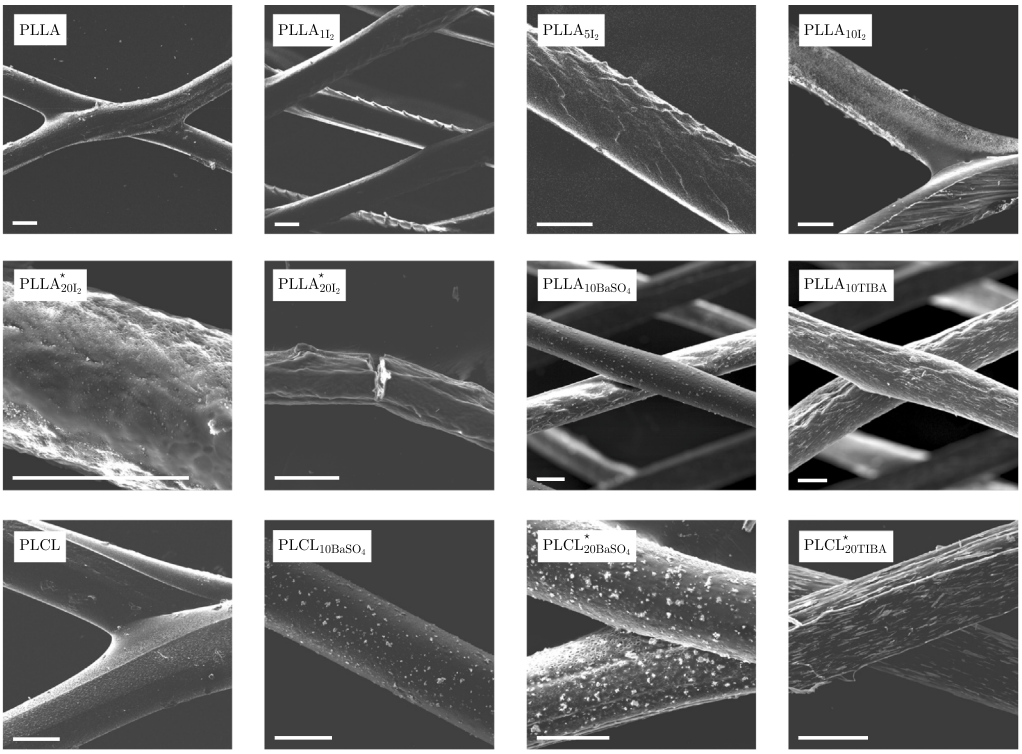

Fig. 8. SEM images of printed stents. Iodine-containing stents present wave-like surface, with $PLLA^{\star}_{20I_2}$ becoming brittle after thermal treatment. Stents with $BaSO_4$ show dispersion of microparticles and TIBA-containing stents show TIBA crystals in the printing direction. Scale bar corresponds to 100 μm.

by the Absorb, DESolve, Fortitude, Acute, Magmaris, Xinsorb, Art Pure, Ideal or ReZolve stents, all of them equal or greater than 150 μm [49]. The current tendency is to shift towards thinner struts in order to minimize blood turbulence which may lead to thrombotic events. In consequence, more recent designs aim at 125 μm such as the Fantom, or even below 100 μm as the Magnitude or the Falcon [50]. In SC-DW, strut thickness can be further reduced by using thinner micronozzles. The use of a 200 μm diameter nozzle instead of the one with 250 μm allows for a significant reduction in strut thickness for PLLA stents, from 130 μm down to 80 μm. For radiopaque stents, for instance, $PLCL_{10BaSO_4}$ presented a strut thickness around 200 μm, whereas when using a 200 μm diameter nozzle instead, strut thickness was reduced to 175 μm for $PLCL^{\star}_{20BaSO_4}$.

DSC analysis of as-printed stents showed crystallinity percentage to be around 24%. Posterior thermal treatment above PLLA's glass-transition temperature induced higher crystallinity, close to 30%. Other fabrication techniques such as FDM also render polymeric parts with a low degree of crystallinity, below 5% [51,52]. Crystallinity constitutes a key factor in semicrystalline materials such as PLLA, as it is closely correlated to its mechanical performance. Therefore, subsequent annealing processes are widely applied in order to increase the fraction of ordered phase, which in turn impacts the mechanical properties and the biodegradation kinetics [52–55].

As for the mechanical properties, compression tests with printed stents showed the importance of performing a thermal treatment after fabrication in order to increase by about 70% the resistance to compression at 50% deformation. As expected, mesh density also influenced resistance to compression, as the increase in n_p correlated with higher resistance, up to 0.16 N/mm for thermally-treated stents with $n_p = 20$. Fig. A.2b shows the correlation between resistance to compression at 50% deformation with area coverage. Lee et al. [33] performed a parallel plate compression test on the Absorb BVS at a velocity of 10 mm/min, obtaining a radial force of 2.14 ± 0.03 N at 50% diameter reduction. In comparison, 10p stents presented a radial force of 1.25 ± 0.16 N, 15p of 2.19 ± 0.41 N and 20p of 3.26 ± 0.36 N. Although the test parameters were not exactly the same, these results show that the mechanical properties of SC-DW 15p and 20p stents are similar or superior to those shown by a commercial polymeric stent such as the Absorb BVS.

Regarding elastic recovery rate, the effect of TT is clearly seen, as it increases from 90% up to 95%. Therefore, thermally-treated stents are able to maintain the greatest part of their initial shape after being

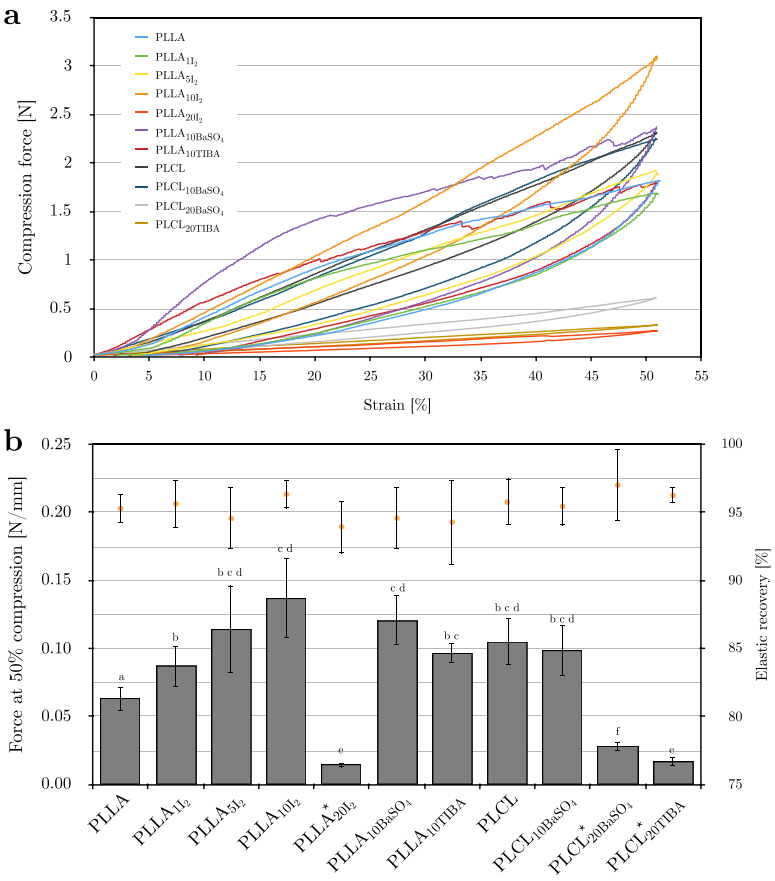

Fig. 9. (a) Compression curves for radiopaque stents. Stents were compressed up to 50% reduction in diameter, with crosshead speed set to 1 mm/min, both in loading and unloading. (b) Force at 50% compression (left axis, bars) and elastic recovery (right axis, dots). Conditions *a*, *b*, *c*, *d*, *e* and *f* are statistically different ($p < 0.05$).

compressed up to 50% deformation with respect to their original diameter. These results are in accordance with the analysis carried out by Zhao et al. in [56], where poly(p-dioxanone) braided stents were tested. Elastic recovery rate was found to be between 86% and 92%, and increased after performing an annealing treatment. Long-term elastic recovery may be studied under cyclic loading assays [57]. Stent's elasticity is a key factor in stent design, as stents must accompany arteries contraction and expansion in order to keep blood flowing [58]. As for the expansion tests, deployment of stents resulted in a good attachment to the silicone artery and showed no signs of collapse. Regardless of the number of peaks, stents were able to withstand pressures up to 16 atm with no signs of strut breakage or detachment among struts, which corresponded to a stent inner radius of 3.26 mm.

In vitro indirect cytotoxicity test with HUVECs indicated that PLLA printed stents were not cytotoxic. Although traces of chloroform may have an impact for non-treated stents, results showed a percentage of living cells well above 80%. This percentage is even higher for thermally-treated stents and equal to or greater than 100%. These results demonstrate the feasibility of the SC-DW approach, even using organic solvents such as chloroform.

As expected, strut thickness had an influence on the thrombogenicity response of studied stents: the thicker the struts, the more thrombogenicity was detected on PLLA stents. The amount of material in contact with the bloodstream was a crucial parameter to control and thus, thinner struts were better. Kolandaivelu et al. showed that 162 μm-strut DES were 1.5-fold more thrombogenic than otherwise identical stents with 81 μm struts [59]. Moreover, in the same study, thick-strut stents implanted in porcine coronary arteries presented more thrombus and fibrin deposition than thin-strut stents at 3 days after implantation, with approximately 60% more thrombus formation [59]. A finite element analysis study of the effect of different stent strut thickness with ISR demonstrated that thinner strut stent resulted in lower stresses in the vessel wall, which is hypothesized to be responsible for the lower restenosis outcome [60]. Finally, the presence of pores distributed on the outer part of the stent did not show to have an impact on stent thrombosis.

The promising results on PLLA stents regarding mechanical and biological properties, together with the versatility of the SC-DW approach, allowed for its modification to render stents radiopaque, with $BaSO_4$ as a positive control for radiopacity. By mixing radiopaque agents into the polymeric solution in chloroform, printable inks with very similar rheological properties to the original ink were obtained. Thermal treatment for iodine-containing stents resulted in a sharp color change, from brownish to pale white. We attribute this variation to the evaporation of iodine molecules, as physical entrapment between PLLA chains may not be enough to avoid their release in gas form due to sublimation. On the other hand, TIBA and $BaSO_4$-containing stents showed no visual alteration after undergoing TT.

Optical microscopy analysis showed a substantial increase in strut thickness with respect to PLLA or PLCL stents when adding a radiopaque agent and printed with the same nozzle. This increase may be associated to the physical presence of iodine, TIBA or $BaSO_4$ microparticles, which hamper the optimal folding for polymeric chains. Strut thickness could be reduced by using a thinner extrusion micronozzle of 200 μm, thus achieving thicknesses comparable to those of commercial stents, as previously discussed. $PLLA^{\star}_{20I_2}$ stents' brittleness arose most probably from iodine evaporation, as it accounted for 20 wt%, which left a fragile structure with thin struts. This effect may be the case as well for other iodine-containing stents, although the higher strut thickness and the lower iodine content might have concealed it. Wave-like surface found for iodine-containing stents is most probably due to extrusion instabilities, as the flux was not as constant as for the original

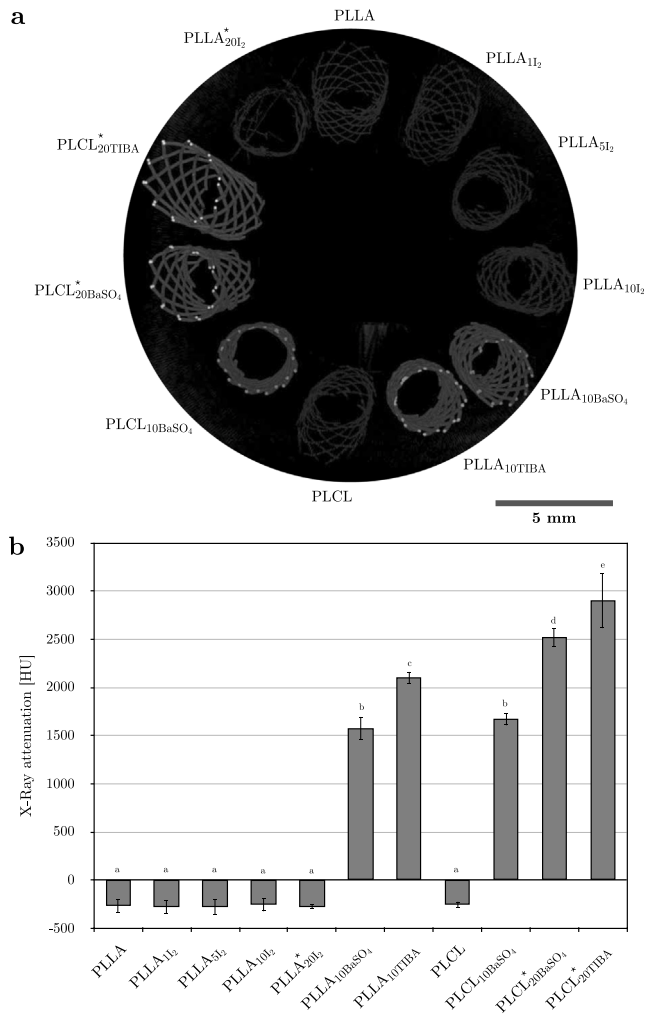

Fig. 10. (a) Stents' reconstruction after microCT scan, being white more radiopaque. (b) X-ray attenuation values for radiopaque stents. Conditions *a*, *b*, *c*, *d* and *e* are statistically different ($p < 0.05$).

PLLA ink. $BaSO_4$ microparticles rendered a rough surface, whereas TIBA crystals formed along the printing direction.

Regarding DSC curves analysis, the addition of iodine did not result in a change in crystallinity for 1 or 5 wt% iodine, but higher iodine contents resulted in a crystallinity increase, especially for $PLLA^{\star}_{20I_2}$. Crystallinity was also higher for $PLLA_{10TIBA}$ than for $PLLA_{10BaSO_4}$, possibly due to the physical constraints shown by $BaSO_4$ microparticles. PLCL stents crystallinity remained fairly constant for $PLCL_{10BaSO_4}$ and $PLCL^{\star}_{20BaSO_4}$, with the exception of $PLCL^{\star}_{20TIBA}$, which showed a substantial increase. Although crystallinity plays a role in the mechanical properties, crush resistance tests showed that the main contribution to compression force was strut thickness. One can clearly distinguish from the compression curves between stents printed with a 250 μm or a 200 μm micronozzle. Therefore, there is a clear correlation between compression force and strut thickness, which in this case is proportional to surface area coverage, given that the stent design is constant (n_p = 10). $PLLA_{10I_2}$ presents the highest normalized force, above 0.13 N/mm, and the highest strut thickness, close to 250 μm.

$BaSO_4$ addition resulted in a significant reinforcement of PLLA, as previously reported [61,62], although at the expense of a discontinuous profile during compression testing. Visual inspection of compressed stents evidenced no strut fracture, although some junctions presented detached struts. This behavior was similar for $PLLA_{10TIBA}$. In contrast, PLCL-based stents compression curves were smooth and presented no such behavior. PLCL was chosen as an alternative to PLLA for its well-described additional flexibility given by the caprolactone monomers, while keeping the same overall stiffness. In fact, PLCL stents show a higher force at 50% compression (0.105 ± 0.017 N/mm vs. 0.063 ± 0.008 N/mm for PLLA) with comparable strut thickness.

Expansion assays confirmed that the discontinuous profile found for $PLLA_{10BaSO_4}$ and $PLLA_{10TIBA}$ was due to partial strut detachment rather than fracture. Unrestricted assays showed that junctions at both ends of the stent separated with increasing pressure, but central junctions remained linked. We attribute this spatial pattern to the SC-DW fabrication process. Upon extrusion, filaments are deposited onto the rotating mandrel and start to solidify as chloroform evaporates. If the filament underneath is too dry, welding between filaments is not strong enough. Therefore, chloroform evaporation is a key process parameter in order to render stents with fused unions between struts. This could be achieved by controlling the atmosphere in which stents are manufactured. All other stents showed no strut fracture or detachment up to 16 atm, which corroborated the close relationship between compression and expansion tests in terms of mechanical properties.

As previously discussed, the presence of iodine entrapped in the stents after heat treatment is probably very low due to its evaporation. This claim is supported by X-ray imaging evidence, as there is no difference in terms of X-ray attenuation for iodine-containing stents with respect to PLLA and PLCL controls. In contrast, iodine atoms bonded in TIBA result in a significant increase in X-ray attenuation, as well as barium atoms for $BaSO_4$-containing stents. Degradation of a selected group of radiopaque PLLA-based stents showed no changes in X-ray attenuation after 3 months incubation, therefore ensuring X-ray visibility in the mid-term. Finally, compression tests of degraded stents showed no changes in terms of mechanical properties with respect to fresh stents, with the exception of $PLLA_{10TIBA}$, which showed a significant decrease in compression force. This may be linked to the particular orientation of TIBA crystals along the filament, which may accelerate PLLA degradation following TIBA dissolution.

Concerning cytotoxicity assays, the addition of iodine or $BaSO_4$ did not result in a cytotoxic effect to cells. Previous studies have investigated iodine's antibacterial effect [9,13,63,64], showing antibacterial properties and biocompatibility both *in vitro* and *in vivo*. Regarding $BaSO_4$, *in vivo* studies showed good biocompatibility of $BaSO_4$-containing PLA urethral, pancreatic and biliary stents [21–23], where $BaSO_4$ microparticles would be excreted through the gastrointestinal tract. TIBA-containing stents showed a certain degree of cytotoxicity for pure extract, although subsequent dilutions attenuated such effect. This outcome may result as a consequence of the chosen sterilization method, which was UV radiation. It has been reported that TIBA presents photodegradation under exposure to UV radiation [65,66], which may result in the appearance of toxic species. In order to confirm this, a new cytotoxicity assay was performed using ethanol soaking as an alternative sterilization method. In this case, cell viability was found to be over 70% for pure extract and subsequent dilutions for the $PLCL^{\star}_{20TIBA}$ (87.6 ± 12.5 % for pure extract, 76.6 ± 10.6 % for dilution $^1/_2$ and 83.8 ± 5.8 % for dilution $^1/_{10}$). This result is in accordance with TIBA's reported biocompatibility in literature [19], where exposure of the different extract concentrations of the TIBA-infused sutures had no effect on Hela cells. Therefore, TIBA's cytotoxic effect is attributed to the photodegradation induced by UV radiation, which may be circumvented by using alternative sterilization methods.

5. Conclusions

In this work we have developed a novel, versatile SC-DW printing system onto a rotating mandrel to manufacture bioresorbable stents. Chloroform-based PLLA ink presented the required shear-thinning behavior for extrusion through a micronozzle. A variety of designs with different mesh patterns and densities were successfully fabricated and

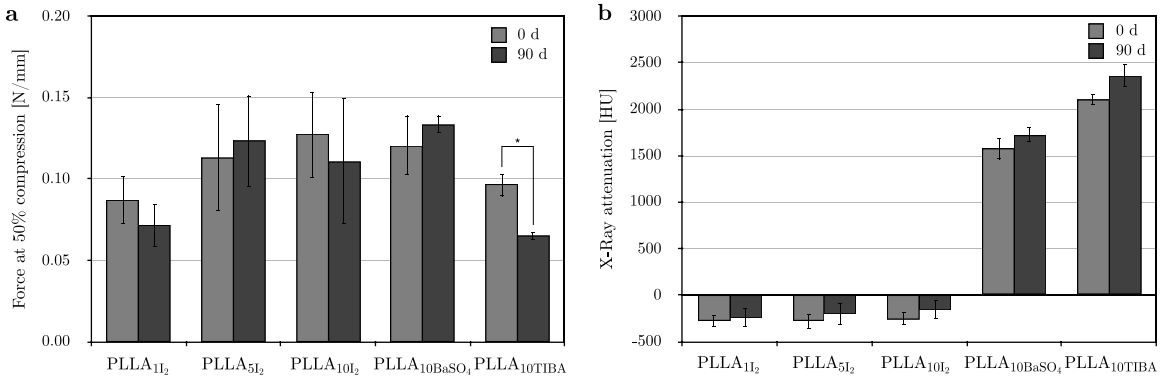

Fig. 11. (a) Force at 50% compression of fresh and incubated stents and (b) X-ray attenuation values of fresh and incubated stents. Statistically significant differences among conditions are shown with an asterisk ($p < 0.05$).

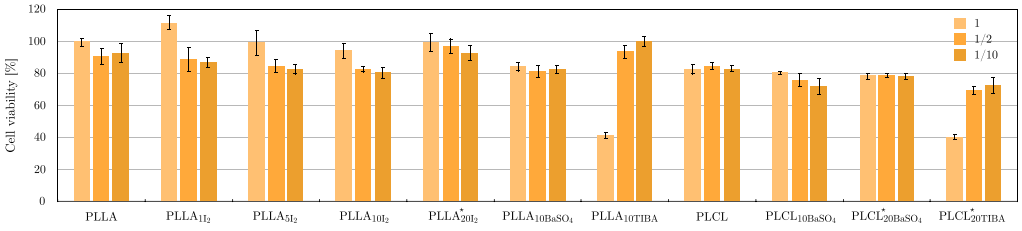

Fig. 12. Cell viability test performed on printed stents for pure extract and dilutions 1/2 and 1/10.

characterized, with encouraging results regarding mechanical and biological properties. The versatility of the SC-DW approach allowed for ink modification in order to obtain radiopaque polymeric stents. MicroCT analysis evidenced increased X-ray attenuation for TIBA- and $BaSO_4$-containing stents with respect to control PLLA or PLCL stents, showing maintained radiopacity after 3 months incubation time.

This preliminary study constitutes a promising starting point in regards of the SC-DW technique's potential for BRS fabrication. The versatility of the approach allows for patient-specific customization in terms of material and printing design in order to achieve sufficient mechanical support with suitable degradation rate. Furthermore, stents with supplementary features may be obtained, such as radiopaque BRS. Future perspectives include the addition of antiproliferative drug into the stents and monitor its release, or surface functionalization with peptides in order to enhance endothelial cell adhesion.

CRediT authorship contribution statement

Victor Chausse: Conceptualization, Investigation, Methodology, Writing – original draft. **Romain Schieber:** Conceptualization, Investigation, Methodology. **Yago Raymond:** Conceptualization, Investigation, Methodology. **Brian Ségry:** Investigation. **Ramon Sabaté:** Investigation. **Kumaran Kolandaivelu:** Conceptualization, Methodology, Supervision. **Maria-Pau Ginebra:** Supervision, Funding acquisition. **Marta Pegueroles:** Conceptualization, Writing – review & editing, Supervision, Formal analysis, Funding acquisition.

Declaration of competing interest

No author associated with this paper has disclosed any potential or pertinent conflicts which may be perceived to have impending conflict with this work. For full disclosure statements refer to https://doi.org/10.1016/j.addma.2021.102392.

Acknowledgments

Financial support was received from Spanish Government, MINECO/FEDER (RTI2018-098075-B-C21), and the Agency for Administration of University and Research Grants (AGAUR) of the Government of Catalonia (2017SGR-1165). This work was supported by the project BASE3D 001-P-001646, co-financed by the European Union Regional Development Fund within the framework of the ERDF Operational Program of Catalonia 2014-2020 with a grant of 50% of total cost eligible. V.C. thanks the Generalitat de Catalunya for the 2019FI-B00627 scholarship. Support for the research of M-P.G. was received through the prize "ICREA Academia" for excellence in research, funded by the Generalitat de Catalunya.

Appendix A. Supplementary data

Supplementary material related to this article can be found online at https://doi.org/10.1016/j.addma.2021.102392.

References

[1] H. Ang, J. Ng, H. Bulluck, P. Wong, S. Venkatraman, Y. Huang, N. Foin, Fundamentals of bioresorbable stents, in: Functionalised Cardiovascular Stents, Elsevier, 2018, pp. 75–97.
[2] G.W. Stone, R. Gao, T. Kimura, D.J. Kereiakes, S.G. Ellis, Y. Onuma, W.-F. Cheong, J. Jones-McMeans, X. Su, Z. Zhang, et al., 1-year outcomes with the absorb bioresorbable scaffold in patients with coronary artery disease: a patient-level, pooled meta-analysis, Lancet 387 (10025) (2016) 1277–1289.
[3] S. Cassese, R.A. Byrne, G. Ndrepepa, S. Kufner, J. Wiebe, J. Repp, H. Schunkert, M. Fusaro, T. Kimura, A. Kastrati, Everolimus-eluting bioresorbable vascular scaffolds versus everolimus-eluting metallic stents: a meta-analysis of randomised controlled trials, Lancet 387 (10018) (2016) 537–544.
[4] S.G. Ellis, D.J. Kereiakes, G.W. Stone, et al., Everolimus-eluting bioresorbable vascular scaffolds in patients with coronary artery disease: Absorb iii trial 2-year results, in: Annual Meeting of the American College of Cardiology, Vol. 18, 2017.
[5] J. Wiebe, H.M. Nef, C.W. Hamm, Current status of bioresorbable scaffolds in the treatment of coronary artery disease, J. Am. Coll. Cardiol. 64 (23) (2014) 2541–2551.
[6] S. McMahon, N. Bertollo, E.D.O. Cearbhaill, J. Salber, L. Pierucci, P. Duffy, T. Dürig, V. Bi, W. Wang, Bio-resorbable polymer stents: a review of material progress and prospects, Prog. Polym. Sci. 83 (2018) 79–96.

[7] J. Fernández, A. Etxeberria, J.-R. Sarasua, Synthesis, Structure and properties of poly (l-lactide-co-ε-caprolactone) statistical copolymers, J. Mech. Behav. Biomed. Mater. 9 (2012) 100–112.

[8] G. Leibundgut, A novel, radiopaque, bioresorbable tyrosine-derived polymer for cardiovascular scaffolds.

[9] K. de Arruda Almeida, A.A.A. de Queiroz, O.Z. Higa, G.A. Abraham, J. San Román, Macroporous poly (ε-caprolactone) with antimicrobial activity obtained by iodine polymerization, J. Biomed. Mater. Res. Part A: An Official J. Soc. Biomater. 68 (3) (2004) 473–478.

[10] B. Nottelet, J. Coudane, M. Vert, Synthesis of an x-ray opaque biodegradable copolyester by chemical modification of poly (ε-caprolactone), Biomaterials 27 (28) (2006) 4948–4954.

[11] J.-M. Coutu, A. Fatimi, S. Berrahmoune, G. Soulez, S. Lerouge, A new radiopaque embolizing agent for the treatment of endoleaks after endovascular repair: Influence of contrast agent on chitosan thermogel properties, J. Biomed. Mater. Res. Part B: Appl. Biomater. 101 (1) (2013) 153–161.

[12] A. Galperin, D. Margel, J. Baniel, G. Dank, H. Biton, S. Margel, Radiopaque iodinated polymeric nanoparticles for x-ray imaging applications, Biomaterials 28 (30) (2007) 4461–4468.

[13] S.I. Goreninskii, K.S. Stankevich, A.L. Nemoykina, E.N. Bolbasov, S.I. Tverdokhlebov, V.D. Filimonov, A first method for preparation of biodegradable fibrous scaffolds containing iodine on the fibre surfaces, Bull. Mater. Sci. 41 (4) (2018) 100.

[14] K. Lei, W. Shen, L. Cao, L. Yu, J. Ding, An injectable thermogel with high radiopacity, Chem. Commun. 51 (28) (2015) 6080–6083.

[15] K. Lei, Y. Chen, J. Wang, X. Peng, L. Yu, J. Ding, Non-invasive monitoring of in vivo degradation of a radiopaque thermoreversible hydrogel and its efficacy in preventing post-operative adhesions, Acta Biomater. 55 (2017) 396–409.

[16] X. Li, N. Anton, G. Zuber, M. Zhao, N. Messaddeq, F. Hallouard, H. Fessi, T.F. Vandamme, Iodinated α-tocopherol nano-emulsions as non-toxic contrast agents for preclinical x-ray imaging, Biomaterials 34 (2) (2013) 481–491.

[17] D. Mawad, L.A. Poole-Warren, P. Martens, L.H. Koole, T.L. Slots, C.S.v. Hooy-Corstjens, Synthesis and characterization of radiopaque iodine-containing degradable pva hydrogels, Biomacromolecules 9 (1) (2007) 263–268.

[18] R. Samuel, E. Girard, G. Chagnon, S. Dejean, D. Favier, J. Coudane, B. Nottelet, Radiopaque poly (ε-caprolactone) as additive for x-ray imaging of temporary implantable medical devices, RSC Adv. 5 (102) (2015) 84125–84133.

[19] B. Singhana, A. Chen, P. Slattery, I.K. Yazdi, Y. Qiao, E. Tasciotti, M. Wallace, S. Huang, M. Eggers, M.P. Melancon, Infusion of iodine-based contrast agents into poly (p-dioxanone) as a radiopaque resorbable ivc filter, J. Mater. Sci.: Mater. Med. 26 (3) (2015) 124.

[20] F. Zhao, H. Xu, W. Xue, Y. Li, J. Sun, F. Wang, G. Jiang, L. Li, L. Wang, Iodinated poly (p-dioxanone) as a facile platform for x-ray imaging of resorbable implantable medical devices, J. Biomater. Appl. 35 (1) (2020) 39–48.

[21] T. Isotalo, E. Alarakkola, M. Talja, T. Tammela, T. Välimaa, P. Törmälä, Biocompatibility testing of a new bioabsorbable x-ray positive sr-pla 96/4 urethral stent, J. Urol. 162 (5) (1999) 1764–1767.

[22] T. Lämsä, H. Jin, J. Mikkonen, J. Laukkarinen, J. Sand, I. Nordback, Biocompatibility of a new bioabsorbable radiopaque stent material (ba so4 containing poly-l, d-lactide) in the rat pancreas, Pancreatology 6 (4) (2006) 301–305.

[23] J. Laukkarinen, I. Nordback, J. Mikkonen, P. Kärkkäinen, J. Sand, A novel biodegradable biliary stent in the endoscopic treatment of cystic-duct leakage after cholecystectomy, Gastrointest. Endosc. 65 (7) (2007) 1063–1068.

[24] A. Scafa Udriste, A.-G. Niculescu, A.M. Grumezescu, E. Bădilă, Cardiovascular stents: A review of past, current, and emerging devices, Materials 14 (10) (2021) 2498.

[25] C. Pan, Y. Han, J. Lu, Structural design of vascular stents: A review, Micromachines 12 (7) (2021) 770.

[26] R.A. Buiten, E.H. Ploumen, P. Zocca, C.J. Doggen, L.C. Van Der Heijden, M.M. Kok, P.W. Danse, C.E. Schotborgh, M. Scholte, F.H. De Man, et al., Outcomes in patients treated with thin-strut, very thin-strut, or ultrathin-strut drug-eluting stents in small coronary vessels: a prespecified analysis of the randomized bio-resort trial, JAMA Cardiol. 4 (7) (2019) 659–669.

[27] P. Guedeney, B.E. Claessen, R. Mehran, D.E. Kandzari, M. Aquino, S. Davis, L. Tamis, J.C. Wang, I. Othman, O.S. Gigliotti, et al., Small-vessel pci outcomes in men, women, and minorities following platinum chromium everolimus-eluting stents: Insights from the pooled platinum diversity and promus element plus post-approval studies, Catheter. Cardiovasc. Interv. 94 (1) (2019) 82–90.

[28] N. Bink, V.B. Mohan, S. Fakirov, Recent advances in plastic stents: A comprehensive review, Int. J. Polym. Mater. Polym. Biomater. 70 (1) (2021) 54–74.

[29] A.B. AlAli, M.F. Griffin, Butler, Three-dimensional printing surgical applications, Eplasty 15 (2015).

[30] J. Goole, K. Amighi, 3d printing in pharmaceutics: A new tool for designing customized drug delivery systems, Int. J. Pharm. 499 (1–2) (2016) 376–394.

[31] R. Van Lith, E. Baker, H. Ware, J. Yang, A.C. Farsheed, C. Sun, G. Ameer, 3d-printing strong high-resolution antioxidant bioresorbable vascular stents, Adv. Mater. Technol. 1 (9) (2016) 1600138.

[32] S.A. Park, S.J. Lee, K.S. Lim, I.H. Bae, J.H. Lee, W.D. Kim, M.H. Jeong, J.-K. Park, In vivo evaluation and characterization of a bio-absorbable drug-coated stent fabricated using a 3d-printing system, Mater. Lett. 141 (2015) 355–358.

[33] S.J. Lee, H.H. Jo, K.S. Lim, D. Lim, S. Lee, J.H. Lee, W.D. Kim, M.H. Jeong, J.Y. Lim, I.K. Kwon, et al., Heparin coating on 3d printed poly (l-lactic acid) biodegradable cardiovascular stent via mild surface modification approach for coronary artery implantation, Chem. Eng. J. 378 (2019) 122116.

[34] A.J. Guerra, J. Ciurana, 3d-printed bioabsorbable polycaprolactone stent: The effect of process parameters on its physical features, Mater. Des. 137 (2019) 430–437.

[35] A.J. Guerra, P. Cano, M. Rabionet, T. Puig, J. Ciurana, 3d-printed pcl/pla composite stents: Towards a new solution to cardiovascular problems, Materials 11 (9) (2018) 1679.

[36] C.J. Boyer, M. Boktor, H. Samant, L.A. White, Y. Wang, D.H. Ballard, R.C. Huebert, J.E. Woerner, G.E. Ghali, J.S. Alexander, 3d printing for bio-synthetic biliary stents, Bioengineering 6 (1) (2019) 16.

[37] R. Schieber, Y. Raymond, C. Caparrós, J. Bou, E. Herrero Acero, G.M. Guebitz, C. Canal, M. Pegueroles, Functionalization strategies and fabrication of solvent-cast plla for bioresorbable stents, Appl. Sci. 11 (4) (2021) 1478.

[38] J. Bruneaux, D. Therriault, M.-C. Heuzey, Micro-extrusion of organic inks for direct-write assembly, J. Micromech. Microeng. 18 (11) (2008) 115020.

[39] S.-Z. Guo, M.-C. Heuzey, D. Therriault, Properties of polylactide inks for solvent-cast printing of three-dimensional freeform microstructures, Langmuir 30 (4) (2014) 1142–1150.

[40] E. Fischer, H.J. Sterzel, G. Wegner, Investigation of the structure of solution grown crystals of lactide copolymers by means of chemical reactions, Kolloid-Z. Z. Polym. 251 (11) (1973) 980–990.

[41] ISO 25539-2, Cardiovascular Implants. Endovascular Devices. Part 1: Vascular Stents, International Organization for Standardization, 2012.

[42] H. Kahraman, M. Ozaydin, E. Varol, S.M. Aslan, A. Dogan, A. Altinbas, M. Demir, O. Gedikli, G. Acar, O. Ergene, The diameters of the aorta and its major branches in patients with isolated coronary artery ectasia, Tex. Heart Inst. J. 33 (4) (2006) 463.

[43] K. Kolandaivelu, E.R. Edelman, Low background and pulsatile, in vitro flow circuit for modeling coronary implant thrombosis, J. Biomech. Eng. 124 (6) (2002) 662–668.

[44] K. Kolandaivelu, E.R. Edelman, Environmental influences on endovascular stent platelet reactivity: an in vitro comparison of stainless steel and gold surfaces, J. Biomed. Mater. Res. Part A 70 (2) (2004) 186–193.

[45] ISO 10993-5, Biological Evaluation of Medical Devices — Part 5: Tests for in Vitro Cytotoxicity, International Organization for Standardization, 2009.

[46] ISO 10993-12, Biological Evaluation of Medical Devices — Part 12: Sample Preparation and Reference Materials, International Organization for Standardization, 2007.

[47] S.-Z. Guo, F. Gosselin, N. Guerin, A.-M. Lanouette, M.-C. Heuzey, D. Therriault, Solvent-cast three-dimensional printing of multifunctional microsystems, Small 9 (24) (2013) 4118–4122.

[48] Y. Cheng, P. Gasior, K. Ramzipoor, C. Lee, J.C. McGregor, G.B. Conditt, T. McAndrew, G.L. Kaluza, J.F. Granada, In vitro mechanical behavior and in vivo healing response of a novel thin-strut ultrahigh molecular weight poly-l-lactic acid sirolimus-eluting bioresorbable coronary scaffold in normal swine, Int. J. Cardiol. 286 (2019) 21–28.

[49] H.Y. Ang, H. Bulluck, P. Wong, S.S. Venkatraman, Y. Huang, N. Foin, Bioresorbable stents: Current and upcoming bioresorbable technologies, Int. J. Cardiol. 228 (2017) 931–939.

[50] D. Capodanno, Bioresorbable scaffolds in coronary intervention: unmet needs and evolution, Korean Circ. J. 48 (1) (2018) 24–35.

[51] M.A. Cuiffo, J. Snyder, A.M. Elliott, N. Romero, S. Kannan, G.P. Halada, Impact of the fused deposition (fdm) printing process on polylactic acid (pla) chemistry and structure, Appl. Sci. 7 (6) (2017) 579.

[52] R.A. Wach, P. Wolszczak, A. Adamus-Wlodarczyk, Enhancement of mechanical properties of fdm-pla parts via thermal annealing, Macromol. Mater. Eng. 303 (9) (2018) 1800169.

[53] T.R. Welch, R.C. Eberhart, J. Reisch, C.-J. Chuong, Influence of thermal annealing on the mechanical properties of plla coiled stents, Cardiovasc. Eng. Technol. 5 (3) (2014) 270–280, http://dx.doi.org/10.1007/s13239-014-0189-3.

[54] J. Sarasua, N. López-Rodríguez, E. Zuza, S. Petisco, B. Castro, M. Del Olmo, T. Palomares, A. Alonso-Varona, Crystallinity assessment and in vitro cytotoxicity of polylactide scaffolds for biomedical applications, J. Mater. Sci.: Mater. Med. 22 (11) (2011) 2513–2523.

[55] N. Vasanthan, O. Ly, Effect of microstructure on hydrolytic degradation studies of poly (l-lactic acid) by ftir spectroscopy and differential scanning calorimetry, Polym. Degrad. Stab. 94 (9) (2009) 1364–1372.

[56] F. Zhao, W. Xue, F. Wang, C. Yu, H. Xu, Y. Hao, L. Wang, A new approach to improve the local compressive properties of ppdo self-expandable stent, J. Mech. Behav. Biomed. Mater. 68 (2017) 318–326.

[57] H. Jaziri, S. Mokhtar, N. Chakfe, F. Heim, S.B. Abdessalem, Elastic recovery of polymeric braided stents under cyclic loading: preliminary assessment, J. Mech. Behav. Biomed. Mater. 98 (2019) 131–136.

[58] A. Freitas, M. de Araujo, W. Zu, R. Fangueiro, Development of weft-knitted and braided polypropylene stents for arterial implant, J. Text. Inst. 101 (12) (2010) 1027–1034.

[59] K. Kolandaivelu, R. Swaminathan, W.J. Gibson, V.B. Kolachalama, K.-L. Nguyen-Ehrenreich, V.L. Giddings, L. Coleman, G.K. Wong, E.R. Edelman, Stent thrombogenicity early in high-risk interventional settings is driven by stent design and deployment and protected by polymer-drug coatings, Circulation 123 (13) (2011) 1400–1409.

[60] H. Zahedmanesh, C. Lally, Determination of the influence of stent strut thickness using the finite element method: implications for vascular injury and in-stent restenosis, Med. Biol. Eng. Comput. 47 (4) (2009) 385.

[61] I.M. de Arenaza, N. Sadaba, A. Larrañaga, E. Zuza, J. Sarasua, High toughness biodegradable radiopaque composites based on polylactide and barium sulphate, Eur. Polym. J. 73 (2015) 88–93.

[62] J.-P. Nuutinen, C. Clerc, P. Törmälä, Mechanical properties and in vitro degradation of self-reinforced radiopaque bioresorbable polylactide fibres, J. Biomater. Sci., Polymer Edition 14 (7) (2003) 665–676.

[63] T. Shirai, T. Shimizu, K. Ohtani, Y. Zen, M. Takaya, H. Tsuchiya, Antibacterial iodine-supported titanium implants, Acta Biomater. 7 (4) (2011) 1928–1933.

[64] H. Tsuchiya, T. Shirai, H. Nishida, H. Murakami, T. Kabata, N. Yamamoto, K. Watanabe, J. Nakase, Innovative antimicrobial coating of titanium implants with iodine, J. Orthop. Sci. 17 (5) (2012) 595–604.

[65] R. Jarboe Jr., J. Data, J. Christian, Photodisintegration studies of 14c-carboxyl 2, 3, 5-triiodobenzoic acid, J. Pharm. Sci. 57 (2) (1968) 323–325.

[66] S. Allard, J. Criquet, A. Prunier, C. Falantin, A. Le Person, J.Y.-M. Tang, J.-P. Croué, Photodecomposition of iodinated contrast media and subsequent formation of toxic iodinated moieties during final disinfection with chlorinated oxidants, Water Res. 103 (2016) 453–461.